CHAPTER 5

CERIUM SUBSTITUTED Y-TYPE BARIUM HEXAFERRITE (Co_2-Y); AS A HETEROGENEOUS CATALYST FOR REDUCTION OF TOXIC NITRO-ORGANIC POLLUTANTS

5.1 Introduction

The industries utilize various toxic organic compounds like nitroaromatic compounds, phenols, aromatic hydrocarbons, and sulphonamides as a precursor, solvents, or intermediates. The direct disposal of this industrial wastage to the environment causes severe threats to human health and aquatic life. It is essential to remove these nitroaromatic compounds from the wastewater to make it more ecological. Several soft ferrite materials are being studied for their catalytic activities for the reduction of nitroaromatic compounds as heterogeneous catalysts. Due to the limitations of thermal and chemical stability in soft ferrite, Y-type barium hexaferrite material can be proposed as a replacement for these soft ferrite materials due to their excellent chemical and thermal stability with better corrosion resistance.

The cerium-substituted Y-type barium hexaferrite $Ba_2Co_2Fe_{12-x}Ce_xO_{22}$ (x = 0.0, 0.1, 0.2, & 0.3) are synthesized using the nitrate-based sol-gel auto combustion method and investigated their catalytic efficiency within the reduction of nitroaromatic-compounds, one of the significant water contaminants. The proposed hexaferrite samples are prepared using the analytical grades of barium nitrate [$Ba(NO_3)_2$], cobalt nitrate [$Co(NO_3)_3.6H_2O$], ferrous nitrate [$Fe(NO_3)_3.9H_2O$], cerium nitrate [$Ce(N0_3)_3.6H_2O$] as elemental precursors and citric acid [$C_6H_8O_7 \cdot H_2O$] as a chelating agent or fuel within the process. The selection of cerium as a substituting element is inspired by enhanced catalytic reduction efficiencies of earlier studied cerium-added systems. It is found that the Ce substitution significantly enhances the catalytic activity for the selective reduction of nitrogen monoxide by propene [(Yokoyama and Misono, 1994)]. The CeO_2, along with Sm_2O_3, improves the catalytic activity for the reduction of 4-nitrophenol [(Pinheiro *et al.*, 2019)]. The Ce complexes with organic ligands in the presence of 1% Pd/C increase the hydrogenation of nitroaromatic compounds [(Shebaldova *et al.*, 1979)]. The nickel nitrate-supported CeO_2 provides a 12

times faster reduction of the 4-nitrophenol than the nickel oxide substrate [(Vivek, Arunkumar, and Suresh Babu, 2016)]. The addition of CeO_2 to the SnO_2 may provide superior catalytic activity for the selective reduction of nitro-compounds within the existence of hydrazine hydrate as a hydrogen donor [(Jyothi *et al.*, 1999)]. The Fe-doped CeO_2 can effectively catalyze the reduction of NO by CO [(Hou *et al.*, 2018)]. The influence of catalyst amount, solvent, reaction time & temperature, and amount of hydrazine needed to complete the conversion of nitrobenzene to aniline is observed with the pure Co_2-Y ferrite. The catalytic functioning of the Co_2-Y hexaferrite powder is evaluated based on the isolated yield of aniline in the final reaction product through the column-chromatography separation method. The influence of Ce substitution at the iron site for the aniline selectivity is also investigated in optimized situations.

The selective reduction of nitrobenzene and other derivatives is evaluated within the water as a solvent in the presence of hydrazine monohydrate (2 mmol) as the hydrogen source. Initially, nitrobenzene (1 mmol), hydrazine hydrate (2 mmol, 64 mg), and a suitable amount of catalyst powder ($Ba_2Co_2Fe_{12-x}Ce_xO_{22}$) with an excess amount of water as a reaction medium are added within a sealed reaction tube. This mixture is allowed to heat at around 100°C for 12 hrs with uninterrupted stirring. The thin-layer chromatography (TLC) is employed to monitor the end of the reaction. The reaction mixture is permitted to cool down to room temperature and utilized for product confirmation. The organic layer is extracted by dissolving with water and ethyl-acetate. This extracted layer is dried above anhydrous Na_2SO_4, and the solvent is vaporized under reduced pressure to achieve the crude product. At last, this crude product is diluted with ethyl-acetate or hexane and separated using silica-gel-based column chromatography and confirmed by proton NMR (^{1}H NMR) and $^{13}C\{^1H\}$ NMR spectra.

5.2 Results and discussion

The room temperature XRD pattern of the calcined Ce-substituted barium hexaferrite powder is shown in Fig. 5.1(a). It is revealed that all these samples consist of a single crystalline Y-type barium hexaferrite phase. All the peaks acquired in the XRD pattern match precisely with the peak positions of the reference JCPDS card no-440206 [(Suthar *et al.*, 2020)], which confirms the formation of a single-phase hexagonal $Ba_2Co_2Fe_{12}O_{22}$ having an *R-3m* space group. No traces of any impurity phase have been found in these samples by substituting iron with cerium. Correspondingly, the XRD pattern elucidates a successful cerium substitution on the iron sites of Y-type barium hexaferrite lattice. The average crystallite size, lattice parameters, *c/a* ratio, unit cell volume, and X-ray density are calculated and tabulated in Table 5.1, including surface area, total pore volume, and mean pore diameter.

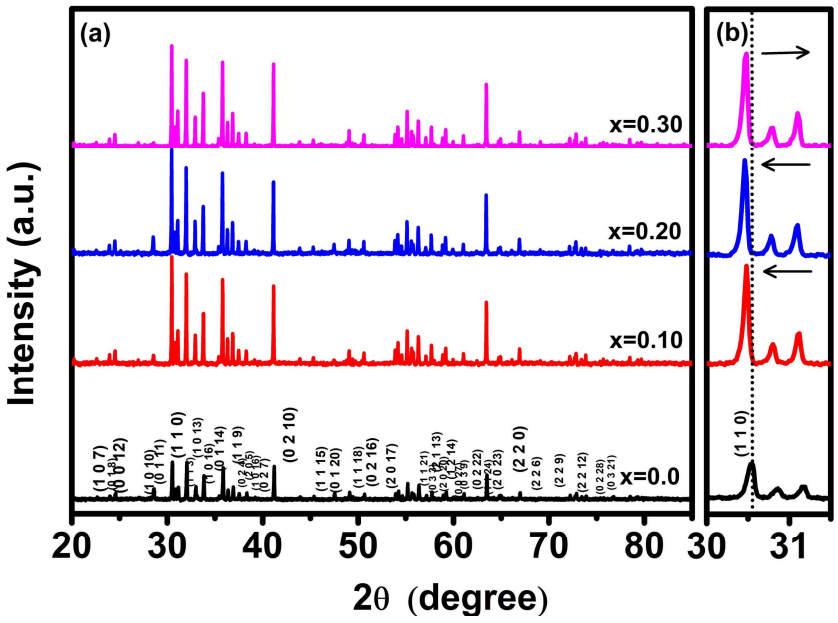

Figure 5.1 XRD pattern of calcined $Ba_2Co_2Fe_{12-x}Ce_xO_{22}$ (x = 0.0, 0.1, 0.2, & 0.3) ferrite powders.

It is found that the crystallite size is in the range of 60-72 nm. The replacement of Ce^{3+} with Fe^{3+} causes enhancement in the lattice parameter, resulting in a slight expansion

of unit cell volume up to x = 0.2. It may be explained based on the difference in the ionic radii. The substitution of a larger Ce^{3+} ion (r = 1.05 Å) at the place of a smaller Fe^{3+} (r = 0.64 Å) ion leads to a positive difference in the ionic radius, which can explain a slight expansion in the unit cell [(Almessiere, Slimani, and Baykal, 2018), (Vakil *et al.*, 2015), (Pawar *et al.*, 2015)]. Further addition of Ce^{3+} (x = 0.3) results in a slight contraction to the unit cell. This reverse situation can be explained due to diffusion inhibition of rare-earth elements in magnetoplumbite structure [(Almessiere, Slimani, and Baykal, 2018), (Thakur, Singh, and Barman, 2013)]. It may suggest the limits of solubility of substituted Ce in the composition. A minor peak shifting (Fig. 5.1(b)) is observed towards the left side up to the x = 0.2 and then towards the right side in the x = 0.3 composition. The X-ray density also shows an increasing trend due to the higher atomic mass of Ce^{3+} compared to the host Fe^{3+}. The addition of cerium results in an increase in the surface area and rising total pore volume, along with decreasing the mean pore diameter on the surface.

Table 5.1 Crystallite size, lattice parameters, *c/a* ratio, unit cell volume, X-ray density, surface area, total pore volume and mean pore diameter of calcined $Ba_2Co_2Fe_{12-x}Ce_xO_{22}$ (x = 0.0, 0.1, 0.2, & 0.3) ferrite powders.

Composition	Crystallite size (nm)	Lattice parameters (Å)		*c/a*	Unit Cell volume ($Å^3$)	X-ray density (g/cm^3)	Surface area (m^2g^{-1})	Total pore volume (At P/P_0 = 0.990) (cm^3/g)	Mean pore diameter (nm)
		a	*c*						
x = 0.0	72.35	5.861	43.458	7.415	1292.84	5.451	37.1	0.00243	22.676
x = 0.1	68.23	5.865	43.555	7.426	1297.49	5.462	38.4	0.00360	21.162
x = 0.2	66.59	5.869	43.570	7.424	1299.71	5.486	40.9	0.00362	11.330
x = 0.3	60.11	5.868	43.571	7.425	1299.34	5.521	42.3	0.00581	10.619

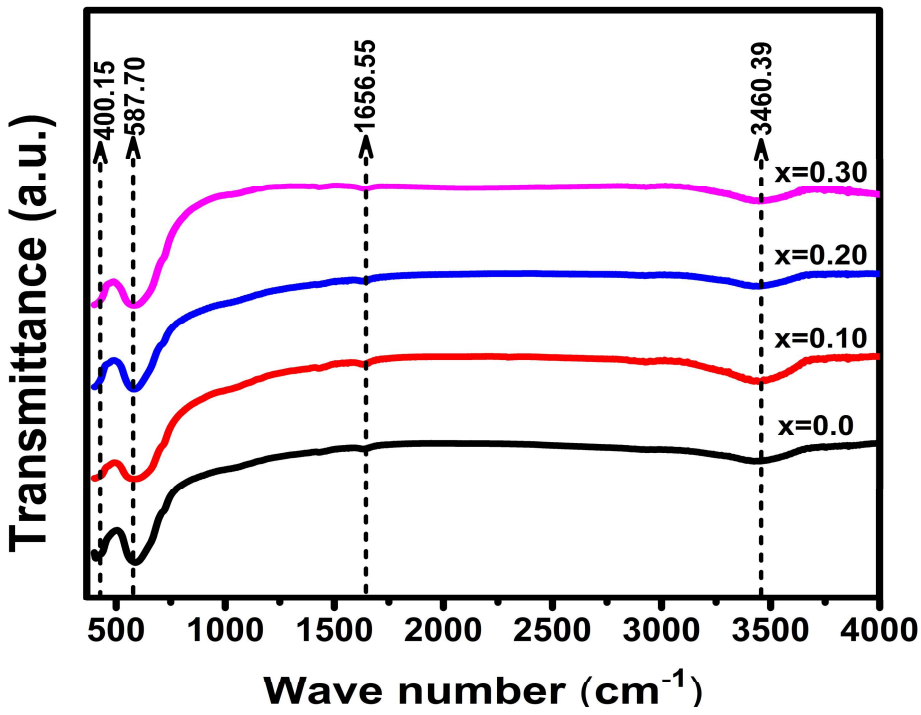

Figure 5.2 FT-IR spectra of calcined $Ba_2Co_2Fe_{12-x}Ce_xO_{22}$ (x = 0.0, 0.1, 0.2, & 0.3) ferrite powders.

Table 5.2 Wave number, effective mass, force constant, and bond length of calcined $Ba_2Co_2Fe_{12-x}Ce_xO_{22}$ (x = 0.0, 0.1, 0.2, & 0.3) ferrite powders.

Composition	Wave number (cm^{-1})	Effective mass (10^{-26} kg)	Force constant, (N/cm)	Bond length (Fe–O) (Å)
x = 0.0	587.7003	2.0648	2.5329	1.8862
x = 0.1	584.8076	2.0648	2.5080	1.8924
x = 0.2	582.3970	2.0648	2.4875	1.8977
x = 0.3	583.3613	2.0648	2.4956	1.8956

The FTIR is engaged in assessing the chemical-bonding and structural variations in the as-produced ferrite powders calcined at 1200°C, as shown in Fig. 5.2. It reveals that all the synthesized samples consist of two major absorption bands in the range 400 cm^{-1} and 600^{-1}. These two characteristic bands refer to metal cations' asymmetric stretching at

octahedral and tetrahedral lattice sites, respectively. In the case of Co_2-Y ferrite, these bands are accredited to the cationic vibrations present in the spinel block [(Suthar *et al.*, 2020), (Adeela *et al.*, 2016)]. It has been noticed that with increasing cerium substitution, these characteristics band shifts toward the low wavenumber up to x = 0.2. It may be due to substituting the larger Ce^{3+} ion with the smaller Fe^{3+} ion, which alters the cation-anion enlargement at octahedral and tetrahedral lattice sites. The force-constant (F) and bond lengths (L_b) of Fe-O are determined and tabulated in Table 5.2.

It is revealed that the substitution of cerium leads to an increase in the bond lengths up to x = 0.2 and also approves the volumetric expansion of unit cell, as obtained in the XRD pattern. Apart from these, two additional absorption peaks are also found in Fig. 5.2. The peak around 1656.55 cm^{-1} represents the O-H-O scissors bending or N–H band due to the use of ammonia-solution while adjusting the pH value [(Zhuang *et al.*, 2020)]. Another absorption peak around 3460 cm^{-1} can be recognized as O–H stretching-vibrations of H_2O, which is due to the moisture content in the samples [(Lalegani and Nemati, 2015), (Shanmugavel *et al.*, 2015)].

Table 5.3 Magnetic parameters N_{BM}, M_s, M_r, M_r/M_s, H_c, and K_1 of calcined $Ba_2Co_2Fe_{12-x}Ce_xO_{22}$ (x = 0.0, 0.1, 0.2, & 0.3) ferrite powders.

Composition	N_{BM} (μB)	M_s (emu/g)	M_r (emu/g)	Squareness Ratio (M_r/M_s)	H_c (Oe)	K_1 (HA^2/kg)
x = 0.0	8.52	33.63	4.50	0.134	21.72	0.0365
x = 0.10	8.42	33.06	2.29	0.069	22.36	0.0369
x = 0.20	7.98	31.15	3.30	0.106	25.58	0.0398
x = 0.30	7.83	30.37	3.07	0.101	35.51	0.0539

The substitution of Ce^{3+} ions substantially impacts the room temperature magnetic properties of substituted Co_2-Y ferrite. Fig. 5.3 shows the magnetic hysteresis behavior of calcined $Ba_2Co_2Fe_{12-x}Ce_xO_{22}$ (x = 0.0, 0.1, 0.2, & 0.3) ferrite powders under the externally applied field of 70 kOe at 300 K. All these ferrite samples display a typical hysteresis-loop, which confirms the ferrimagnetic-behavior. The obtained magnetic parameters such as the number of Bohr magneton (N_{BM}), saturation magnetization (M_s), magnetic retentivity (Mr), squareness ratio (Mr/Ms), coercivity (Hc), magnetic anisotropy constant (K_1) are calculated, and tabulated in Table 5.3.

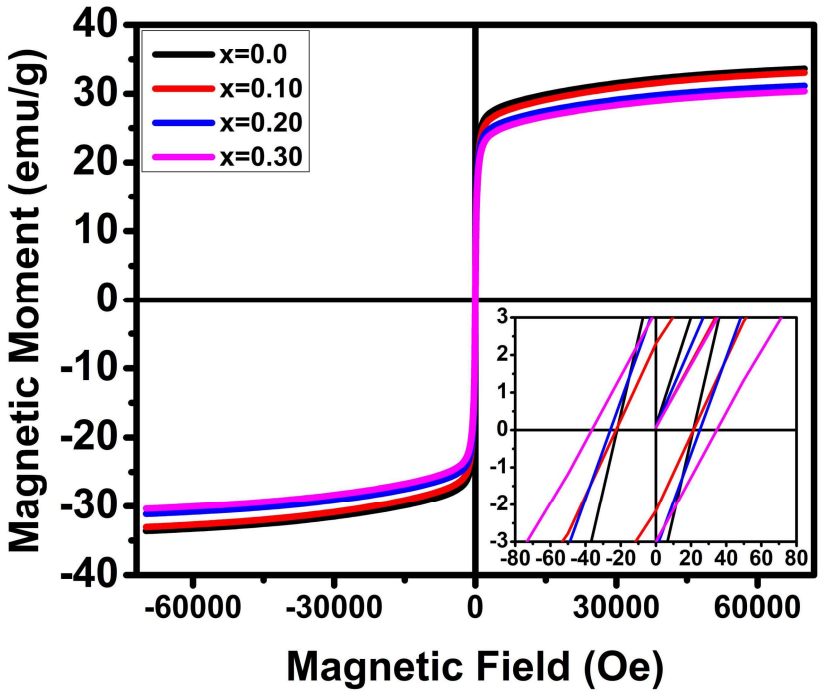

Figure 5.3 Initial magnetization (M versus H) plot of calcined $Ba_2Co_2Fe_{12-x}Ce_xO_{22}$ (x = 0.0, 0.1, 0.2, & 0.3) ferrite powders at room temperature.

The substitution of cerium continuously decreases the effective number of Bohr magneton (N_{BM}) along with saturation magnetization (M_s). It may be due to the replacement of high magnetic moment iron (Fe^{3+} = 5μB) with a low magnetic moment cerium (Ce^{3+} = 1μB) ion [(Pawar *et al.*, 2015), (Suman and Sharma, 2007), (Araz, 2019)]. The results also

suggest that the substitution of Ce^{3+} decreases the magnetization from 33.63 emu/g at x = 0.0 to 30.37 emu/g at x = 0.30 composition. Similar magnetization trend has been observed for $SrFe_{12-x}Ce_xO_{19}$ with ($0.0 \leq x \leq 0.5$) [(Almessiere, Slimani and Baykal, 2018)], $BaFe_{12-x}Ce_xO_{19}$ with ($0.0 \leq x \leq 0.3$) [(Pawar *et al.*, 2015)], $SrFe_{12-x}Nd_xO_{19}$ with ($0.0 \leq x \leq 1.0$) [(Thakur, Singh and Barman, 2013)]. It is well known that the magnetization behavior of any hexaferrites materials depends on the factors affecting the strength of super-exchange interaction within Fe^{3+}-O-Fe^{3+} [(HAN *et al.*, 2012)]. The larger size of the Ce^{3+} ion at the place of the smaller Fe^{3+} ion enlarges the distance between these magnetic ions, which reduces the super-exchange interactions. Additionally, the incorporation of Ce^{3+} ions into the structure causes local strains, which results in non-collinear ferromagnetic stacking or structural disorders [(Almessiere, Slimani, and Baykal, 2018)]. All these factors can explain the weakening of magnetization within the samples with increasing cerium content.

The remnant magnetization (M_r) shows a random behavior within the range of 4.50 to 2.29 emu/g with an overall decreasing nature in comparison to the pristine $Ba_2Co_2Fe_{12}O_{22}$ ferrite. The ratio of remnant magnetization (M_r) to saturation magnetization (Ms), known as remnant ratio or squareness ($S_R = M_r / M_s$), describes the magnetic hardness of that system. The value of the squareness ratio lies from 0 to 1, and it decides the presence of various inter-grain group exchanges [(Adeela *et al.*, 2016)]. According to Day *et al.*, the squareness value informs the various interactions in nanoparticles [(Day, Fuller, and Schmidt, 1977)]. If the value of "S_R" is below 0.05, it means the nanoparticles are multi-domain nature without any specific orientation, whereas ($0.05 < S_R < 0.5$) refers to the pseudo-single domain nature, and these particles interact with each other through magneto-static coupling. But, ($0.5 < M_r / M_s < 1$) refers to the single domain nature with more anisotropic behavior. The squareness ratios are found to be in the range of 0.069 to 0.134,

which clearly depicts that the particles are magneto-statically coupled pseudo-single domain nature.

The magnetic field intensity required to demagnetize (zero magnetization) the sample can be quantified as the coercivity (H_c) of that material. It is observed that coercivity (H_c) increases from 21.72 to 35.51 Oe with increasing Ce^{3+} content in the structure. This increment of coercive field can be explained on behalf of decreasing crystallite size or increasing magnetic anisotropy constant value [(Vakil *et al.*, 2015), (Pawar *et al.*, 2015), (Mirkazemi *et al.*, 2015)]. According to R. A. Pawar *et al.*, substituting a strong planar magnetic Ce^{3+} ion at the Fe^{3+} site results in a larger magnetic anisotropy constant (K_1) [(Pawar *et al.*, 2015)]. The magnetic anisotropy constant (K_1) is enhanced for all the substituted samples. A larger demagnetizing field is essential to overcome the enlarged anisotropic energy barrier within the substituted sample and results in increased coercivity. Similar results are obtained for M-type barium hexaferrite substituted with a planer magnetic Ce^{3+} ion at the place of Fe^{3+} [(Pawar *et al.*, 2015)].

The catalytic efficiency of as-synthesized $Ba_2Co_2Fe_{12}O_{22}$ hexaferrite powder is considered in the reduction of aromatic nitrobenzene in the presence of hydrazine hydrate as a hydrogen source, which is a widely applicable methodology for the production of aromatic amines. The aniline is the product of concern in this reaction. These ferrites adsorb the nitro compound and hydrazine on the surface. The transition metal ions (Fe^{3+} ion for ferrite) present on the surface help to dissociate the hydrazine, and the H^+ ions further reduce the nitrobenzene to its constituent aniline [(Kim, Kim, and Kim, 2011)]. It is a first attempt to check the candidacy of a hard magnetic ($Ba_2Co_2Fe_{12}O_{22}$) ferrite material, produced via sol-gel auto-combustion route, for the catalytic reduction of nitrobenzene.

A blank reaction is conducted to endorse the necessity of the hexaferrite material for selective reduction of nitrobenzene. It is found that in the absence of the catalyst, the

reaction doesn't propagate. To attain the optimized parameters for this reaction, the isolated yield for the aniline is analyzed for different amounts of pure Y-type barium-hexaferrite powder as a catalyst with nitrobenzene as a reactant and hydrazine hydrate ($N_2H_4 \cdot H_2O$) as a hydrogen source. Hydrazine is an attractive in-situ source of hydrogen, and it is suitable for the large-scale adaptability and generation of harmless byproducts after the completion of the reaction. The hydrated form of hydrazine is utilized within the reaction due to its better stability, safety, and easy handling [(Cantillo, Moghaddam, and Kappe, 2013)]. It provides hydrogen to the reactant and dissociates nitrogen gas and water [(Kim, Kim, and Kim, 2011), (Li, Frett, and Li, 2014), (Shi *et al.*, 2006)]. The amount of catalyst, reaction temperature, reaction time, choice of solvent, choice of a hydrogen source, and amount of hydrogen source is optimized for the proposed reaction. Due to the economic & environmental advantages, inherent safety, and nontoxicity, the most convenient water is designated as a solvent instead of other organic solvents. David Cantillo *et al.* (with iron oxide) and Lei Wang *et al.* (with metallic iron powder) have also promoted the use of water as a solvent [(Cantillo, Moghaddam and Kappe, 2013), (Wang *et al.*, 2003)]. It provides a better conversion (> 99%) and optimum yield for the reduction of nitroaromatic compounds.

Fig. 5.4(a) states the role of catalyst amount on the conversion of nitrobenzene and isolated yield (%) of aniline through the reduction of nitrobenzene. Initially, the conversion increases rapidly and reaches around 99% (nearby the completion of the reaction) with 20 mg of catalyst, but the isolated yield (%) of aniline increases slowly up to 40 mg of catalyst; afterward, it grows rapidly up to the saturation level with 100 mg of catalyst. The increasing trend of aniline selectivity is due to larger reactive sites on the catalyst surface. After reaching a saturation level of catalyst amount, i.e., 100 mg of $Ba_2Co_2Fe_{12}O_{22}$, the isolated yield (%) becomes constant and doesn't affect anymore with the further addition of catalyst.

The saturation level can be explained due to the agglomeration of magnetic particles with a higher amount of catalyst loading in the reaction tube. It is due to the less active sites with lower contact areas of the reactants [(Tong *et al.*, 2016)]. It may also be due to the total reactant within the reaction tube getting saturated with the available active sites on the catalyst's surface, so further addition of a catalyst is not more beneficial [(Yang *et al.*, 2016)]. Therefore, the optimum catalytic amount is 100 mg with hydrazine hydrate as a hydrogen source within the water as a solvent.

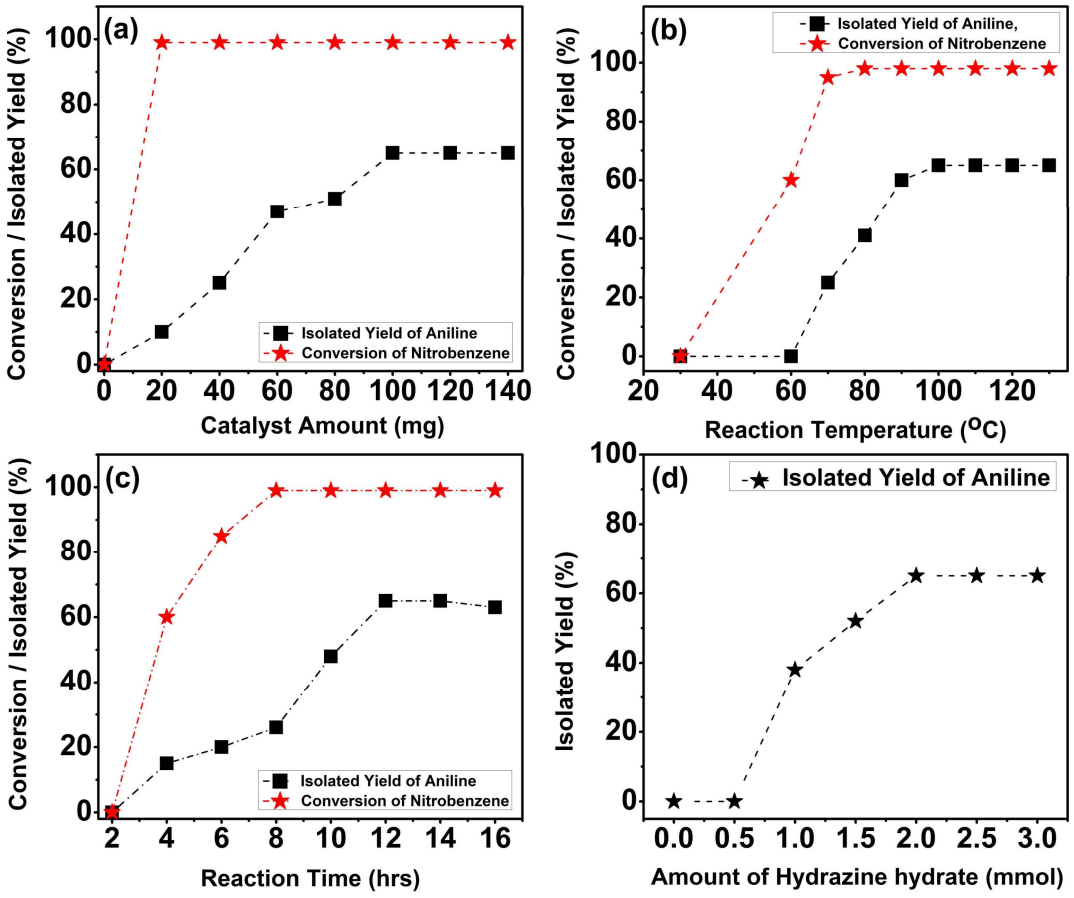

Figure 5.4 Effect of (a) catalyst amount (b) reaction temperature (c) reaction time (d) amount of hydrated hydrazine on reduction of nitrobenzene.

Fig. 5.4(b) elaborates on the impact of the temperature on the percentage conversion of the reactant and isolated yield (%) of aniline in the presence of an optimized amount

(100 mg) of $Ba_2Co_2Fe_{12}O_{22}$ as a catalyst within the range of room temperature to 130˚C. The result shows that the reaction doesn't initiate at a lower temperature (< 60˚C); afterward, it increases dramatically and achieves total conversion (nearby the completion of the reaction) of a reactant at the temperature of 70˚C with an isolated yield of 25% aniline. These outcomes are in good agreement with the earlier studies, where the reaction completion was achieved at 80˚C with $Co_{0.2}Fe_{2.8}O_4$ as a catalyst in the presence of 2.25 mL of $N_2H_4 \cdot H_2O$ [(Yang *et al.*, 2016)]. The maximum selectivity (65%) for aniline is achieved at around 100˚C with a total conversion of nitrobenzene. The increasing temperature of water leads to the decreasing density, dielectric constant, and solubility parameter, but it enhances the dissociation constant (K_w), which allows the easy formation of hydronium (H^+) and hydroxide (OH^-) ions that can help in the reduction mechanism. Thus, the solvent (water)'s increasing temperature can explain the higher selectivity for aniline [(Wang *et al.*, 2003)]. Beyond 100˚C, it shows no further variation in the isolated yield (%) for the concerned product up to 130˚C, as it becomes constant at 65%. With a collective consideration of the energy balance, the total conversion and maximum isolated yield for aniline are at 100˚C for the proposed reaction with 100 mg of catalyst, hydrazine hydrate as a hydrogen source within the water as a solvent.

Fig. 5.4(c) clarifies the role of reaction time on the percentage conversion of the nitrobenzene and isolated yield (%) of aniline in the presence of an optimized amount (100 mg) of $Ba_2Co_2Fe_{12}O_{22}$, with optimized reaction temperature at 100˚C within the range of 2 to 16 hrs at an interval of 2 hrs in each step. The results show that the conversion of nitrobenzene increases dramatically and reaches its maximum value of 99% (nearby the completion of the reaction) at 8 hrs. The isolated yield (%) is found to increase rapidly up to 4 hrs, then its rate of increment becomes slow within the range of 4 hrs to 8 hrs; afterward, it reaches a maximum value of 65% at 12 hrs and becomes constant for further. The minor

reduction at 16 hrs to the isolated yield of aniline may be attributed to the initiation of aniline degradation (formation of formamide) [(Yang *et al.*, 2019)]. The total conversion of nitrobenzene and maximum isolated yield for aniline is optimized with the reaction time of 12 hrs for the proposed reaction with 100 mg of catalyst, hydrazine hydrate as a hydrogen source within the water as a solvent at 100˚C.

Fig. 5.4(d) informs the impact of the various amounts of hydrated hydrazine on the isolated yield (%) of aniline in the optimized conditions. The consideration of hydrated hydrazine amount is an essential concern because the less or insufficient amount may be unable to provide the required amount of hydrogen to the reactant, and the excess amount may affect the environmental health adversely. The results suggest that the best performance is achieved at 2 mmol of hydrated hydrazine, considered as an optimum value corresponding to the isolated yield of 65% for aniline in nitrobenzene reduction. The use of hydrazine hydrate within the proposed reaction facilitates the process in terms of easy handling and generation of eco-friendly by-product (N_2) as compared to other sources [(Kim, Kim, and Kim, 2011), (Cantillo, Moghaddam and Kappe, 2013)].

Table 5.4 describes the role of various solvents on the isolated yield (%) of aniline in the presence of an optimized amount (100 mg) of $Ba_2Co_2Fe_{12}O_{22}$, reaction temperature at 100˚C, and 12 hrs of reaction. The solvents such as di-oxane, isopropyl alcohol (IPA), toluene, dimethylformamide (DMF), methanol (MeOH), ethanol (EtOH), and water (H_2O) are studied at optimized conditions for the proposed reaction. All the solvents are previously used to reduce nitro compounds [(Jyothi, 2000), (Sun, Quan, and Wang, 2015), (Cantillo, Moghaddam, and Kappe, 2013)]. The solvent plays a crucial role in defining the performance of a catalyst. The results suggest that the Di-oxane, IPA, Toluene, and DMF show a very poor response to the reaction (<40% yield), whereas methanol (MeOH) and ethanol (EtOH) provide a reasonable response (<60% yield), and the water (H_2O) provides

the best results among all the solvents within the optimized conditions. The behavior of water among all these solvents can be explained based on the highest solvent polarity (maximum dielectric constant), which is responsible for the enhanced initial hydrogenation rate and moderate catalytic activity [(Vaidya, Kulkarni and Chaudhari, 2003)].

Table 5.4 Influence of solvent on reduction of nitrobenzene with $Ba_2Co_2Fe_{12}O_{22}$ as a catalyst.

S. No.	Solvent	Catalyst	Catalyst amount (mg)	Hydrogen source (2 mmol)	Temp. (˚C)	Time (hrs)	Yield (%)
1	Di-oxane	$Ba_2Co_2Fe_{12}O_{22}$	100	$NH_2NH_2{\cdot}2H_2O$	100	12	Trace
2	IPA	$Ba_2Co_2Fe_{12}O_{22}$	100	$NH_2NH_2{\cdot}2H_2O$	100	12	20
3	Toluene	$Ba_2Co_2Fe_{12}O_{22}$	100	$NH_2NH_2{\cdot}2H_2O$	100	12	35
4	DMF	$Ba_2Co_2Fe_{12}O_{22}$	100	$NH_2NH_2{\cdot}2H_2O$	100	12	37
5	MeOH	$Ba_2Co_2Fe_{12}O_{22}$	100	$NH_2NH_2{\cdot}2H_2O$	100	12	57
6	EtOH	$Ba_2Co_2Fe_{12}O_{22}$	100	$NH_2NH_2{\cdot}2H_2O$	100	12	54
7	H_2O	$Ba_2Co_2Fe_{12}O_{22}$	100	$NH_2NH_2{\cdot}2H_2O$	100	12	65

(Isolated Yields, Optimised Conditions: Nitrobenzene (1 mmol, 123 mg), $N_2H_2.H_2O$ (2 mmol, 64 mg), Catalyst (100 mg), Temperature 100 °C, Time 12 hrs)

Table 5.5 explains the role of different hydrogen sources on the isolated yield (%) of aniline in the presence of an optimized amount (100 mg) of $Ba_2Co_2Fe_{12}O_{22}$, 100˚C reaction temperature, 12 hrs of reaction time with water as a solvent. The result shows that the hydrated hydrazine ($NH_2NH_2{\cdot}2H_2O$) acts as an excellent hydrogen source among all other combinations likewise isopropyl alcohol (CH_3CHOH) + potassium hydroxide (KOH), formic acid (HCOOH) + triethylamine (TEA), and acetic acid (CH_3COOH) + H_2O. It provides the maximum isolated yield (≈ 65%) for aniline at optimized conditions for the proposed reaction.

Table 5.6 explains the role of cerium content on the catalytic performance of Ce-substituted Y-type barium hexaferrites (Co_2-Y) {$Ba_2Co_2Fe_{12-x}Ce_xO_{22}$ (x = 0.0, 0.1, 0.2, & 0.3)} samples in the isolated yield (%) of aniline in the optimized conditions such as catalyst amount (100 mg), reaction temperature (100˚C), time (12 hrs), hydrogen source (2 mmol of hydrated hydrazine) and water as a solvent. It is clarified that all the synthesized hexaferrite samples can efficiently reduce the nitrobenzene and convert it into a product of concern, i.e., aniline. It is confirmed that incorporating cerium ions leads to the enhancement of isolated yield for aniline up to the x = 0.2 composition. It can also be supported by the increased surface area from 37.1 to 40.9 m^2g^{-1} (Table 5.1) with the addition of cerium from x = 0.0 to x = 0.2 compositions. The rate of nitrobenzene reduction shows a linear dependency on the surface area of the catalyst [(Agrawal and Tratnyek, 1996)].

Table 5.5 Influence of hydrogen source on reduction of nitrobenzene with $Ba_2Co_2Fe_{12}O_{22}$ as a catalyst.

S. No.	Catalyst	Catalyst amount (mg)	Hydrogen source (2 mmol)	Temp. (˚C)	Time (hrs)	Yield (%)
1	$Ba_2Co_2Fe_{12}O_{22}$	100	Isopropyl alcohol (CH_3CHOH) + Potassium hydroxide (KOH)	100	12	35
2	$Ba_2Co_2Fe_{12}O_{22}$	100	Formic acid (HCOOH) + Triethyl amine (TEA)	100	12	00
3	$Ba_2Co_2Fe_{12}O_{22}$	100	Acetic acid (CH_3COOH) + H_2O	100	12	00
4	$Ba_2Co_2Fe_{12}O_{22}$	100	$NH_2NH_2{\cdot}2H_2O$	100	12	65

(Isolated Yields, Optimised Conditions: Nitrobenzene (1 mmol, 123 mg), Catalyst (100 mg), Temperature 100 °C, Time 12 hrs, Solvent: Water)

Afterward, in the case of x = 0.3, the isolated yield (%) has a minor drop with the enhanced surface area value (42.3 m^2g^{-1}). It can be explained due to the decreasing pore diameter. The pore diameter becomes a significant concern in explaining the catalytic activity. The availability of smaller pores on the catalyst surface lowers the reaction rate due to easy blockage or inactivation of these pores. It also provides more hindrance to the diffusion of reactant or reaction product [(Ghampson *et al.*, 2010)]. So, the lower value of isolated yield (%) for aniline can be correlated to the more inactivation or occlusion of pores (may be reached critical pore size), which doesn't allow the reactant to interact with the active sites on the catalyst surface.

Table 5.6 Effect of cerium content on the performance of the catalyst in nitro reduction.

S. No.	Catalyst	Catalyst amount (mg)	Hydrogen source (2 mmol)	Temp. (˚C)	Time (hrs)	Yield (%)
1	$Ba_2Co_2Fe_{12}O_{22}$	100	$NH_2NH_2{\cdot}2H_2O$	100	12	65
2	$Ba_2Co_2Fe_{11.9}Ce_{0.1}O_{22}$	100	$NH_2NH_2{\cdot}2H_2O$	100	12	67
3	$Ba_2Co_2Fe_{11.8}Ce_{0.2}O_{22}$	100	$NH_2NH_2{\cdot}2H_2O$	100	12	73
4	$Ba_2Co_2Fe_{11.7}Ce_{0.3}O_{22}$	100	$NH_2NH_2{\cdot}2H_2O$	100	12	71

(Isolated Yields, Optimised Conditions: Nitrobenzene (1 mmol, 123 mg), $N_2H_2.H_2O$ (2 mmol, 64 mg), Catalyst (100 mg), Temperature 100 °C, Time 12 hrs, Solvent: Water)

The XPS spectra is recorded in the range of 1350 eV to 1 eV region to confirm the chemical composition and the existence of elemental valency in all these calcined Ce-substituted Y-type barium hexaferrites samples used as a catalyst for the proposed reaction. The XPS peaks are deconvoluted to determine the relative contribution of existing transition metal compounds. A broad scan of XPS spectra is shown in Fig. 5.5(a), confirming the existence of Ba, Co, Fe, Ce, and O elements, without any contamination

except carbon in the samples. The respective C1*s* (internal standard) peak is adjusted to 284.8 eV to rectify the binding energy determination for the other peaks [(Wu, Li, and Li, 2015)]. Fig. 5.5(b) demonstrates the deconvoluted high-resolution electronic levels of Ba-3*d* spectra, which are found to have a perfect fit with four peaks positioned at binding energy values of 778.66, 779.87, 794.00, and 795.250 eV. The peaks associated with binding energy (BE) ~779.87 (Ba-3*d*5/2) & 795.250 (Ba-3*d*3/2) are the characteristics of spin-orbit doublet (having energy separation of 15.38 eV) for Ba-3*d* core level. The remaining two peaks situated at lower BE don't depict any other oxidation states of Ba ion. These can be considered as shoulder peaks due to the formation of the relaxation phase, which is responsible for minimizing the surface strain [(Keswani *et al.*, 2017), (Ashraf *et al.*, 2020)].

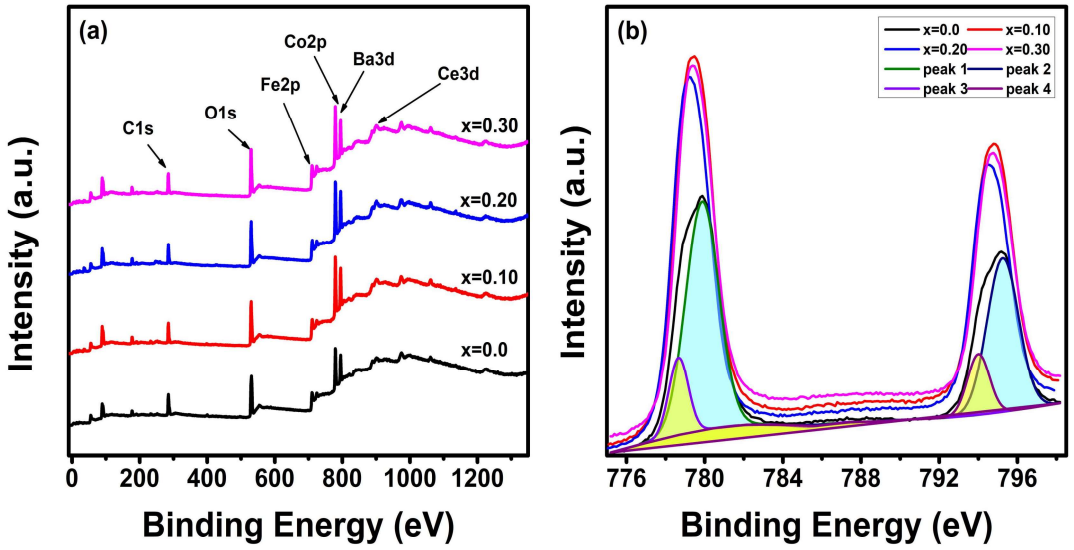

Figure 5.5 (a) The wide scan photoelectron spectra of $Ba_2Co_2Fe_{12-x}Ce_xO_{22}$ (x = 0.0, 0.1, 0.2, & 0.3) surface, (b) high resolution Ba-3*d* spectrum**.**

Fig. 5.6(a) demonstrates the deconvoluted high-resolution electronic levels of Co-2*p* spectrum (780 to 795 eV) for all samples. It is quite intricate to analyze because of the existence of the Ba-3*d* spectrum inside the same limit of binding energies. The existence

of two main peaks allotted to the Co-2*p*3/2 (779.69 eV) and Co-2*p*1/2 (794.95 eV), having an energy difference of 15.26 eV, along with the two satellite peaks at 787.95 eV and 804.14 eV, confirm the characteristic presence of cobalt on the surface of all these samples. Further, the deconvolution of these two characteristic peaks (Co-2*p*3/2 and Co-2*p*1/2) results in two spin-orbit doublets for each, which confirms the co-occurrence of Co^{2+} and Co^{3+} in the samples. These peaks may be assigned to the Co^{3+} -2*p*3/2 (778.68 eV), Co^{2+} -2*p*3/2 (779.88 eV), Co^{3+} -2*p*1/2 (794.22 eV), and Co^{2+} -2*p*1/2 (795.28 eV), respectively [(Huang *et al.*, 2017), (Wang *et al.*, 2017)].

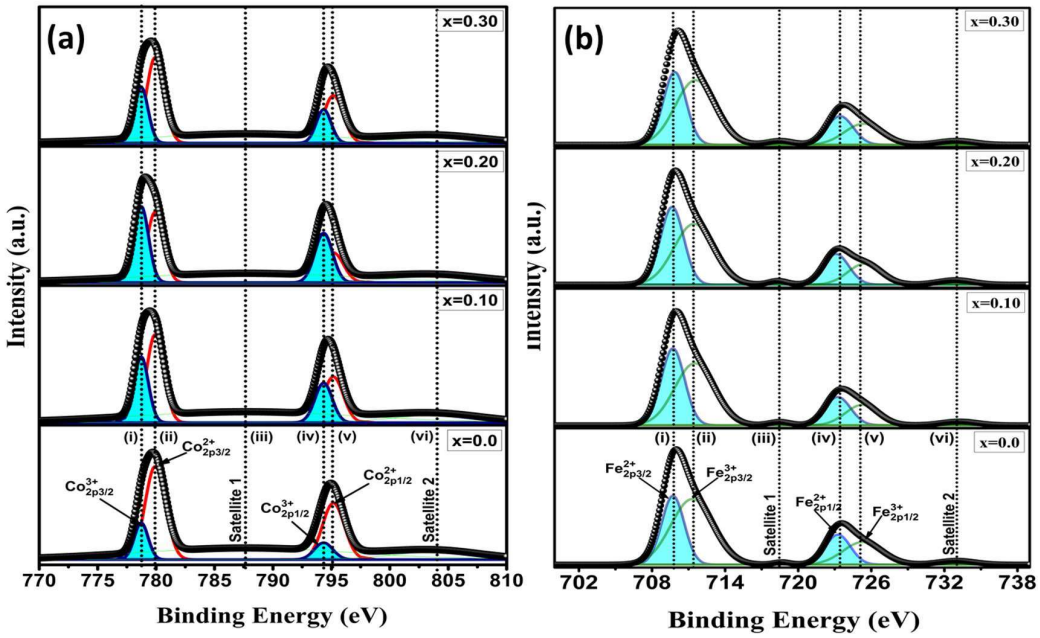

Figure. 5.6 The high-resolution spectra of (a) Co-2*p* and (b) Fe-2*p* for $Ba_2Co_2Fe_{12-x}Ce_xO_{22}$ (x = 0.0, 0.1, 0.2, & 0.3) ferrite samples.

Fig. 5.6(b) reveals the deconvoluted high-resolution electronic levels of Fe-2*p* spectra for all samples. The existence of two prominent peaks assigned to Fe-2*p*3/2 (710.0 eV) and Fe-2*p*1/2 (723.59 eV) having an energy difference of 13.59 eV along with the two satellite peaks at 718.66 eV and 733.02 eV, confirms the characteristic existence of iron on the surface of all these samples. Further, the deconvolution of these two characteristic peaks

(Fe-2*p*3/2 and Fe-2*p*1/2) results in two spin-orbit doublets for each, confirming the co-occurrence of Fe^{2+} and Fe^{3+} in the samples. These four peaks may be assigned to the Fe^{2+}-2*p*3/2 (709.72 eV), Fe^{3+} -2*p*3/2 (711.29 eV), Fe^{2+} -2*p*1/2 (723.26 eV), and Fe^{3+} -2*p*1/2 (725.28 eV), respectively [(Suthar *et al.*, 2020), (Hua *et al.*, 2018)].

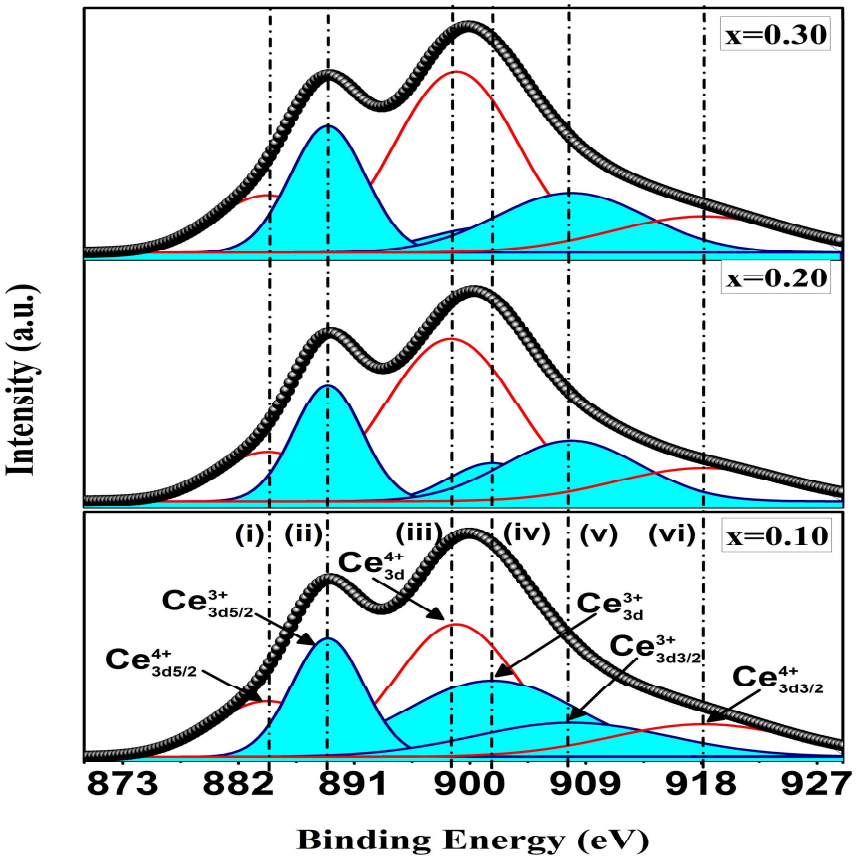

Figure 5.7 The high-resolution Ce-3*d* spectrum for $Ba_2Co_2Fe_{12-x}Ce_xO_{22}$ (x = 0.0, 0.1, 0.2, & 0.3) ferrite samples.

The high-resolution XPS analysis for the Ce-3*d* spectrum, as shown in Fig. 5.7, reveals the existence of both Ce^{3+} and Ce^{4+} in all the substituted samples with two main characteristic peaks for Ce^{4+}-3*d* (898.52 eV) and Ce^{3+} -3*d* (901.75 eV). Further, the deconvolution of the spectrum confirms the presence of two spin-orbit doublets for each of

these prominent peaks, which may be assigned as $Ce^{4+}_{3d5/2}$ (884.2 eV), $Ce^{3+}_{3d5/2}$ (888.9 eV), $Ce^{3+}_{3d3/2}$ (907.8 eV) and $Ce^{4+}_{3d3/2}$ (918.1 eV) [(Suthar *et al.*, 2020), (Chen *et al.*, 2016)].

Fig. 5.8 proves the deconvoluted high-resolution electronic levels of O1*s* spectra for all the samples. It confirms the presence of three main peaks corresponding to crystal lattice oxygen or M-O bonded oxygen (O_i = 529.22 eV), oxygen vacancy (O_{ii} = 530.27 eV), and oxygen associated with hydroxyl group absorbed on the surface (O_{iii} = 532.08 eV) [(Hua *et al.*, 2018), (Kumar *et al.*, 2018), (Jain *et al.*, 2019)]. The overall (both octahedral and tetrahedral sites) relative contribution of Co^{2+}, Co^{3+}, Fe^{2+}, Fe^{3+}, Ce^{3+}, Ce^{4+} ions, and oxygen vacancy (O_{ii}) are determined using peak intensity ratio and described in Table 5.7.

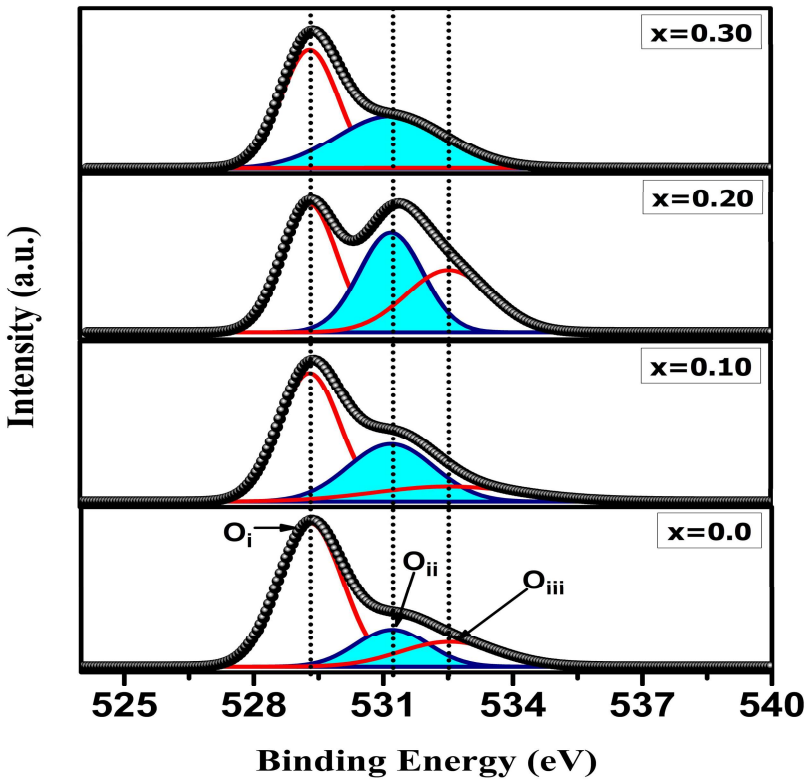

Figure 5.8 The high-resolution O1*s* spectrum for $Ba_2Co_2Fe_{12-x}Ce_xO_{22}$ (x = 0.0, 0.1, 0.2, & 0.3) ferrite samples.

As shown in Table 5.7, the increasing trend for the Fe^{2+} ion concentration up to x = 0.2 and then slight decrement with further addition of cerium can be correlated with the

relative presence of Ce^{4+} and Fe^{2+} ions. The substitution of cerium (Ce^{3+}) to replace the Fe^{3+} ion results in the formation of Fe^{2+} and Ce^{4+} ions according to the following relation:

$$Ce^{3+} + Fe^{3+} \rightarrow Ce^{4+} + Fe^{2+} \quad (5.1)$$

The lattice expansion (revealed from the XRD) and formation of Fe^{2+} ions (revealed from the XPS) are responsible for the creation of oxygen vacancy in the sample [(Chauhan *et al.*, 2019)].

Table 5.7 Surface ionic ratios of the as-prepared samples using XPS.

S. No.	Catalyst	Co^{2+}/ (Co^{2+} + Co^{3+})	Co^{3+}/ (Co^{2+} + Co^{3+})	Fe^{2+}/ (Fe^{2+} + Fe^{3+})	Fe^{3+}/ (Fe^{2+} + Fe^{3+})	Fe^{2+}/Fe^{3+}
1	$Ba_2Co_2Fe_{12}O_{22}$	79.27	20.73	38.70	61.30	0.63
2	$Ba_2Co_2Fe_{11.9}Ce_{0.1}O_{22}$	59.69	40.31	44.55	55.45	0.80
3	$Ba_2Co_2Fe_{11.8}Ce_{0.2}O_{22}$	46.97	53.03	45.36	54.64	0.83
4	$Ba_2Co_2Fe_{11.7}Ce_{0.3}O_{22}$	65.73	34.27	41.58	58.42	0.71

S. No.	Catalyst	Ce^{3+}/ (Ce^{3+} + Ce^{4+})	Ce^{4+}/ (Ce^{3+} + Ce^{4+})	O_{ii}/ (O_i + O_{ii} + O_{iii})
1	$Ba_2Co_2Fe_{12}O_{22}$	0	0	18.67
2	$Ba_2Co_2Fe_{11.9}Ce_{0.1}O_{22}$	50.31	49.69	32.90
3	$Ba_2Co_2Fe_{11.8}Ce_{0.2}O_{22}$	37.85	62.15	33.79
4	$Ba_2Co_2Fe_{11.7}Ce_{0.3}O_{22}$	38.38	61.62	44.58

The oxygen vacancies present on the surface of the catalyst support the catalytic reduction by providing the absolute reactive sites for the reactants, easy dissociation of water molecules into active –OH radicals, facilitating adsorption of hydrogen to the catalytic surface, and lowering the energy barrier for hydrogen bond cleavage [(Wang *et al.*, 2019), (Rodriguez, 2002), (Wang *et al.*, 2018)]. In the case of x = 0.3, the oxygen vacancies keep increasing independently. The excess Ce substitution may generate

compressive stresses to the neighboring space within the lattice, as the XRD results depict an overall contraction of the unit cell. It may be responsible for developing stress-induced oxygen vacancies [(Gopal *et al.*, 2017)]. The enhanced oxygen vacancy concentration may also be supported by the migration of oxygen vacancies toward the surface (to achieve higher stability at the surface with respect to the sub-surface level) [(Han *et al.*, 2019)]. This migration also favors the formation of charged oxygen vacancies having smaller sizes with respect to neutral oxygen vacancies [(Shyichuk and Zych, 2020)]. The possibility of having charged oxygen vacancies supports lattice volume contraction, even at increasing numbers. The ratio of Fe^{2+}/Fe^{3+} can determine the rate of nitro reduction; larger this ratio results in a faster reduction process [(Gorski *et al.*, 2010)]. The presence of maximum Co^{3+} ions (having excellent catalytic activity compared to Co^{2+}) on the catalytic surface also favors the reduction process within this reaction [(Kumar and Gupta, 2017)]. So, the superiority of nitroreduction using $Ba_2Co_2Fe_{11.8}Ce_{0.2}O_{22}$ ferrite can also be supported using XPS data. Due to the maximum achieved aniline selectivity among all the synthesized samples, the $Ba_2Co_2Fe_{11.8}Ce_{0.2}O_{22}$ ferrite is chosen to govern its reproducibility and substrate scope. The best suitable pathway for producing aniline from nitrobenzene within the presence of hydrated hydrazine is shown in Fig. 5.9. It can be explained with three-step mechanisms where the following reactions are responsible (oxidation of hydrated hydrazine) for the generation of $2H^+$ and $2e^-$ for each of the intermediate steps [(Cantillo, Moghaddam, and Kappe, 2013)]:

$$2(Fe^{3+}/Co^{3+}/Ce^{4+}) + N_2H_4 \rightarrow 2(Fe^{2+}/ Co^{2+}/ Ce^{3+}) + 2H^+ + 2e^- + N_2H_2 \quad (5.2)$$

$$N_2H_2 + 2(Fe^{3+}/Co^{3+}/Ce^{4+}) \rightarrow 2(Fe^{2+}/ Co^{2+}/ Ce^{3+}) + 2H^+ + 2e^- + N_2 \quad (5.3)$$

Initially, the nitrobenzene species are adsorbed over the oxygen vacancy-rich surface of barium hexaferrite, where it interacts with the hydrogen ion and releases electrons during the oxidation of hydrazine. In step one, the addition of this double hydrogen-electron pair

with nitrobenzene (Ar-NO_2) results in the first intermediate nitroso benzene (Ar-NO) formation.

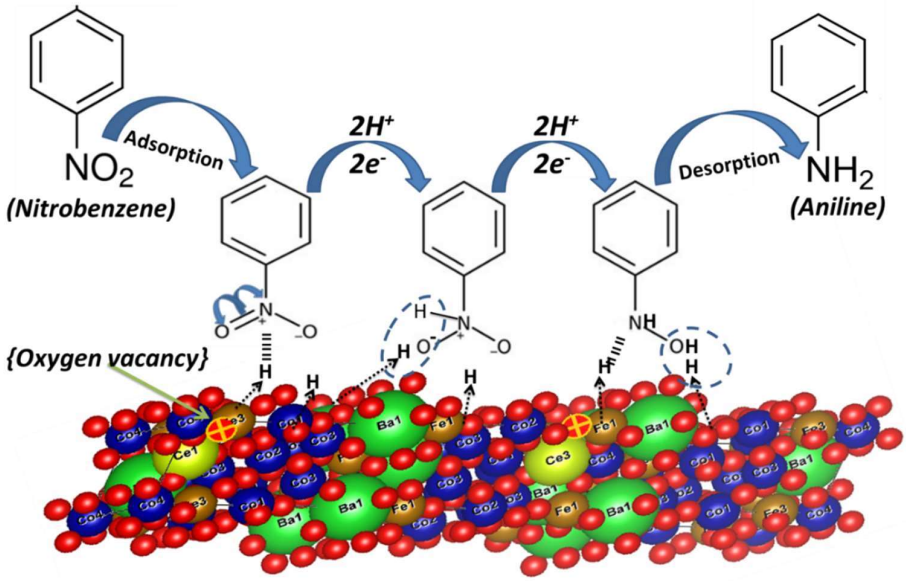

Figure 5.9 Plausible reaction pathway for the reduction of nitrobenzene using $Ba_2Co_2Fe_{11.8}Ce_{0.2}O_{22}$ as a heterogeneous catalyst with hydrated hydrazine.

In the second step, the addition of double hydrogen-electron pair with nitroso benzene (Ar-NO) results in forming a second intermediate hydroxylaminbenzoate (Ar-NHOH). In the last step, the addition of double hydrogen-electron pair with hydroxylaminbenzoate (Ar-NHOH) results in the formation of aniline (Ar-NH_2) [(Cantillo, Moghaddam, and Kappe, 2013), (Larsen *et al.*, 2000)]. As the Co^{3+}, $Fe^{3+,}$ and Ce^{4+} are present over the surface of barium hexaferrite, it reduces during the decomposition of hydrated hydrazine. It oxidizes again while reducing the nitrobenzene to aniline. This proposed redox reaction mechanism may continue up to the total conversion [(Aditya, Pal, and Pal, 2015)].

The microstructure of the calcined $Ba_2Co_2Fe_{11.8}Ce_{0.2}O_{22}$ powder at different magnifications (15K, 25K, and 50K) is shown in Fig. 5.10. SEM micrograph of the calcined

powder reveals that these particles are homogeneous with a nearly hexagonal plate-like shape in a range of 0.4 to 2.6 µm with an average size of 1.4 µm (SD = 0.559).

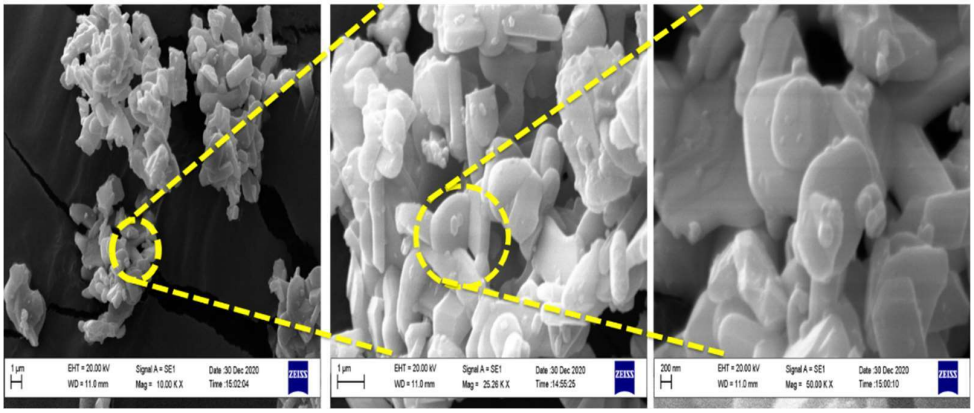

Figure 5.10 SEM micrographs of $Ba_2Co_2Fe_{11.8}Ce_{0.2}O_{22}$ powder at 10K, 25K, and 50K magnification.

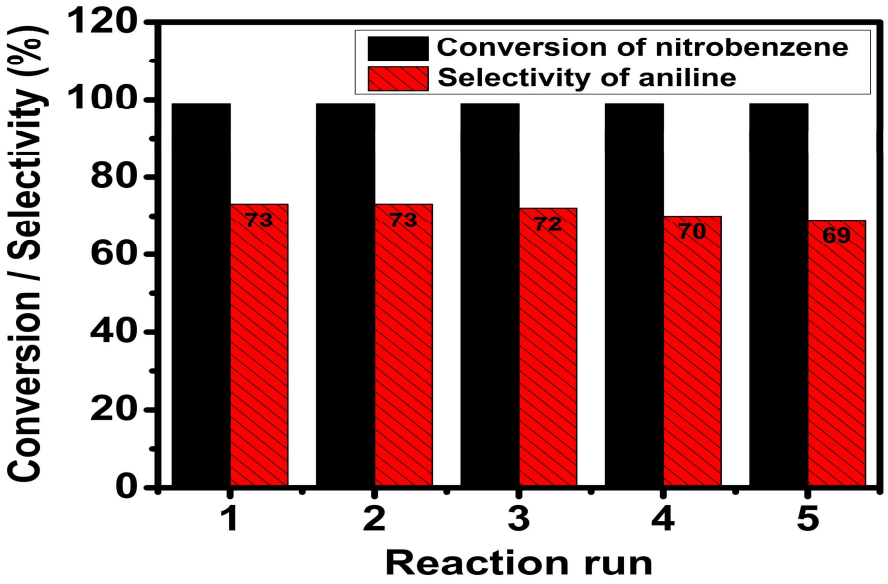

Figure 5.11 Reprocess of the $Ba_2Co_2Fe_{11.8}Ce_{0.2}O_{22}$ ferrite catalyst.

The Ce-substituted Y-type barium hexaferrite ($Ba_2Co_2Fe_{11.8}Ce_{0.2}O_{22}$) is studied the catalytic reproducibility for five consecutive runs with all optimized conditions, as shown in Fig. 5.11.

Table 5.8 Substrates scope for $Ba_2Co_2Fe_{11.8}Ce_{0.2}O_{22}$ ferrite at optimized conditions.

S. No.	Reactants	Products	Isolated Yield (%)
1	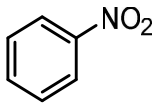	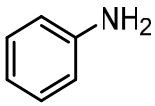	73
2	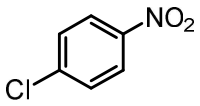	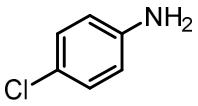	63
3	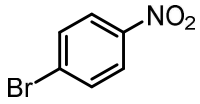	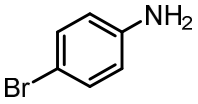	59
4	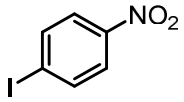	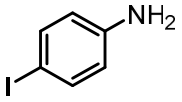	58
5	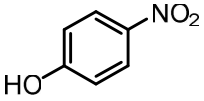	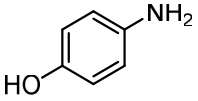	59
6	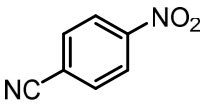	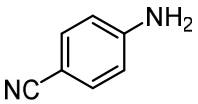	67
7	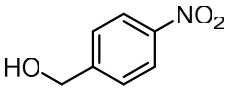	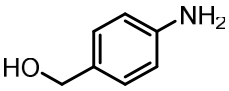	65
8	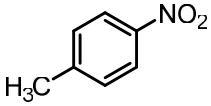	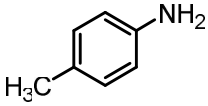	55
9	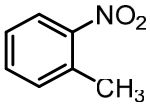	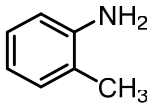	53

It can be easily separated from the reaction mass with the help of an externally applied magnetic field nearby the tube surface. This retrieved catalyst is again utilized for the second run and studied for variation in its catalytic performance during the reaction. A similar process is repeated for up to five trials within the same conditions. It can be concluded that the catalytic reduction efficiency of the as-prepared barium hexaferrite doesn't affect significantly. A minor loss (3-4%) of catalytic activity may be explained due to unavoidable reasons during the handling and separation of catalyst. The results suggest the $Ba_2Co_2Fe_{11.8}Ce_{0.2}O_{22}$ ferrite shows excellent reproducibility for selectivity of aniline within the reduction of nitrobenzene.

Table 5.8 shows the nitro reduction efficiency of $Ba_2Co_2Fe_{11.80}Ce_{0.20}O_{22}$ ferrite along with various substrates within the optimized reaction conditions. The results reveal that it can successfully catalyze the nitroaromatic compounds and convert them into the corresponding aminobenzene. The use of $Ba_2Co_2Fe_{11.80}Ce_{0.20}O_{22}$ as a catalyst provide better selectivity within the production of aniline (73%), 4-chloroaniline (63%), 4-bromoaniline (59%), 4-iodoaniline (58%), 4-aminophenol (59%), 4-aminobenzonitrile (67%), 4-aminophenyl-methanol (65%), p-toluidine (55%), o-toluidine (53%) using constituent nitro compound accordingly.

The reaction product, obtained in a solid/liquid state, is characterized by ^{1}H and ^{13}C NMR spectroscopy; the results confirm the presence of constituting amine by matching the standard peaks (shown in Table 5.9) for all these substrates.

Table 5.9 Confirmation of reaction product obtained with various substrates using ^{1}H and ^{13}C NMR spectra**.**

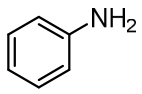	**Aniline [1]** **1H NMR (400MHz, $CDCl_3$)**: δ = 7.16-7.11 (m, 2H), 6.76-6.72 (t, 1H), 6.66-6.64 (t, 2H), 3.56 (s, 2H) **13C NMR (101MHz, $CDCl_3$)**: δ = 146.57, 129.45, 118.66, 115.25
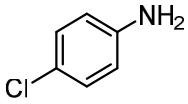	**4-chloroaniline [1]** **1H NMR (400MHz, $CDCl_3$)**: δ = 7.09-7.07 (m, 2H), 6.60-6.57 (m, 2H), 3.64 (s, 2H) **13C NMR (100MHz, $CDCl_3$)**: δ = 145.10, 129.21, 123.16, 116.34
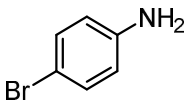	**4-bromoaniline [2]** **1H NMR (400MHz, $CDCl_3$)**: δ = 7.15-7.12 (m, 2H), 6.56-6.52 (m, 2H), 5.26 (s, 2H) **13C NMR (100MHz, DMSO)**: δ = 148.52, 131.85, 116.34, 106.68
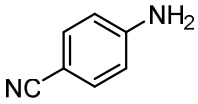	**4-aminobenzonitrile [3]** **1H NMR (400MHz, $CDCl_3$)**: δ = 7.41-7.38 (m, 2H), 6.66-6.63 (m, 2H), 4.28 (s, 2H) **13C NMR (100MHz, $CDCl_3$)**: δ = 150.76, 133.87, 120.45, 114.51, 99.80
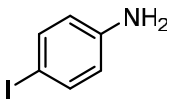	**4-iodoaniline [4]** **1H NMR (400MHz, $CDCl_3$)**: δ = 7.42-7.38 (m, 2H), 6.52-6.45 (m, 2H), 3.54 (s, 2H) **13C NMR (100MHz, $CDCl_3$)**: δ = 146.14, 137.99, 117.38, 79.48
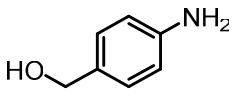	**(4-aminophenyl)methanol [4]** **1H NMR (400MHz, $CDCl_3$)**: δ = 7.17-7.15 (d, 2H), 6.69-6.66 (m, 4H), 4.55 (s, 2H) **13C NMR (100MHz, $CDCl_3$)**: δ = 146.15, 131.09, 128.89, 115.20, 65.42

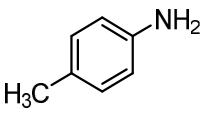	**p-toluidine [4]** **1H NMR (400MHz, $CDCl_3$)**: δ = 6.97-6.94 (d, 2H), 6.60-6.58 (d, 2H), 3.51 (s, 2H), 2.23 (s, 3H) **13C NMR (100MHz, $CDCl_3$)**: δ = 143.94, 129.87, 127.87, 115.37, 20.57
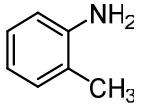	**o-toluidine [5]** **1H NMR (400MHz, $CDCl_3$)**: δ = 7.06-7.02 (t, 2H), 6.73-6.67 (m, 2H), 3.60 (s, 1H), 2.17 (s, 3H) **13C NMR (100MHz, $CDCl_3$)**: δ = 144.62, 130.52, 127.04, 122.41, 118.71, 115.00, 17.45
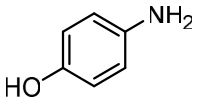	**4-aminophenol [6]** **1H NMR (400MHz, DMSO)**: δ = 8.34 (s, 1H), 6.48-6.40 (m, 4H), 4.39 (s, 2H) **13C NMR (100MHz, DMSO)**: δ =148.73, 141.16, 116.04, 115.74

5.3 Summary

The single-phase Ce-substituted nano-crystalline Y-type barium hexaferrites (Co_2-Y) {$Ba_2Co_2Fe_{12-x}Ce_xO_{22}$ ($0 \leq x \geq 0.30$)} are synthesized using the sol-gel auto-combustion process. The as-prepared ferrite powder can be utilized in a large-scale wastewater treatment plant or industrially conversion of aromatic nitro compounds to the corresponding amine. This work suggests the possible replacement of soft ferrite with a hard ferrite material in the field of catalysis for organic transformation reaction with better performance and mild conditions. The superior performance of the $Ba_2Co_2Fe_{11.8}Ce_{0.2}O_{22}$ ferrite is correlated with the optimum parameters, i.e., maximum Co^{3+} concentration, largest Fe^{2+}/Fe^{3+} ratio, increased surface area, and oxygen vacancy concentration. The optimum conditions are found with the 100 mg $Ba_2Co_2Fe_{11.80}Ce_{0.20}O_{22}$ ferrite as a catalyst loading for 12 hrs of reaction time and 2 mmol of hydrated hydrazine within the water as a solvent at 100 ^oC reaction temperature. All these optimized parameters provide 73% of

aniline selectivity with the total conversion of nitrobenzene. The sample also provides a good magnetic separation without significant loss in the catalytic activity. It makes the process more convenient for large-scale adoption. The Ce-substituted nano-crystalline Y-type barium hexaferrites may be categorized as an efficient catalyst for the organic reduction process due to ease of synthesis, large-scale suitability, and mild process parameters.